# Current-Driven Insulator-To-Metal Transition in Strongly Correlated VO_{2}

Yin Shi and Long-Qing Chen

Phys. Rev. Applied **11**, 014059 — Published 29 January 2019

DOI: 10.1103/PhysRevApplied.11.014059

# Current-Driven Insulator-to-Metal Transition in Strongly Correlated $VO_2$

Yin Shi* and Long-Qing Chen†
*Department of Materials Sciences and Engineering,*
*Pennsylvania State University, University Park, PA 16802, USA*
(Dated: January 6, 2019)

Despite extensive studies on the insulator-to-metal transition (IMT) in strongly correlated $VO_2$, the fundamental mechanism underlying the current-driven IMT in $VO_2$ is still not well understood. Although it has generally been believed that the mechanism is Joule heating leading to a rise in temperature to above its normal transition temperature, there are ample experimental evidences demonstrating that the transition could be driven by nonthermal electronic processes. Here we formulate a phase-field model to demonstrate that the electric current may drive the IMT isothermally via the current-induced electron correlation weakening. We discover that a current with a large density ($\sim 10^1$ nA/nm$^2$) induces a few-nanosecond ultrafast resistive switching, consistent with experimental measurements. We also construct the temperature-current phase diagram and investigate the influence of the current on domain walls. This work is expected to provide guidance for understanding the current-driven IMT in $VO_2$ and for designing $VO_2$-based electric switching devices.

## I. INTRODUCTION

The insulator-to-metal transition (IMT) in the strongly correlated electron system, vanadium dioxide ($VO_2$) [1], has been attracting widespread attention; it not only provides a platform for fundamental scientific research of strong correlation physics [2–4], but also offers potential novel device applications such as sensors, Mott field-effect transistors and memristors [5–9]. Above the transition temperature $T_c = 338$ K [10], $VO_2$ is a metal with a rutile (R) structure while below $T_c$, it turns into an insulator with a monoclinic (M1) structure, at which the resistivity, infrared transmission and eigenstrain change dramatically [11, 12]. Chemical doping [13] or the application of a uniaxial stress [14] can stabilize another monoclinic (M2) insulating phase. The IMT can be induced by various external stimuli including temperature, strain/stress, doping and light [1, 13–15]. It has been experimentally demonstrated that the IMT can also be triggered by an electric voltage (field), which is of particular interest owing to its potential application in information technology [6–9, 16].

Although the electric field alone (in an open circuit) can drive the IMT [6, 16], the electric current commonly accompanying the electric field (in a closed circuit) may also lead to the IMT [17–21]. Unlike in the field-driven IMT that the initial insulating state changes to the equilibrium metallic ground state, in the current-driven IMT the insulating state changes to the nonequilibrium metallic steady state. Two kinetic processes are expected to take place simultaneously in $VO_2$ when it is subject to an electric current: the current heats up the system through Joule heating, and the free carriers injected into the system screen the electron-electron repulsion and thus reduce the electron correlation [22–24]. The Joule heating effect can lead to a rise in temperature to above $T_c$ and thus thermally trigger the IMT. On the other hand, the correlation weakening effect induced by the current may delocalize the electrons in the insulating state, thereby induce the IMT. These two mechanisms are often entangled with each other, complicating the understanding of the underlying mechanisms for the current-driven IMT.

Many experiments and simulations employing dc biases and low-frequency voltage pulses seem to suggest the Joule heating as the main mechanism for the current-driven IMT [25–29]. For example, using the fluorescence spectra of rare-earth doped micron-sized particles as local temperature sensors, Zimmers *et al.* found that the local temperature of the $VO_2$ sample reaches the transition temperature $T_c$ as the IMT is induced by a dc current [28]. Nevertheless, other experiments showed that the transition voltage weakly depends on the thermal dissipation rate and the initial temperature of the $VO_2$ sample, indicating that the IMT is unlikely to be induced by the Joule heating effect [30, 31]. Furthermore, it has been found that the application of a voltage pulse of few volts (accompanied by a corresponding current pulse) switches $VO_2$ from insulator to metal in few or tens of nanoseconds [17, 19, 20]. This ultrafast resistive switching can hardly be attributed to the Joule heating mechanism, since the time scale of the Joule-heating-induced switching is expected to be at least one order larger than the time scale of the switching observed in the experiments [17, 19, 20]. According to these studies, the ultrafast switching must be driven primarily by the correlation weakening effect induced by the current.

Despite extensive experimental studies on the current-induced ultrafast switching, there are still no theoretical models that can be employed to explore the mechanisms underlying the phenomenon. Recently we formulated a phase-field model to describe the IMT in $VO_2$. The thermodynamics is described by a Landau potential as a function of structural and electronic order parameters and free electron and hole densities [32, 33], which

* yxs187@psu.edu
† lqc3@psu.edu

treats the structural distortion and the electron correlation on an equal footing. It has been successfully applied to the determination of equilibrium stable states under strain/stress [32], and under electric fields in an *open circuit* configuration [33]. In this work, this model is further extended to describe the *nonequilibrium* process of the current-driven IMT in mesoscale systems (in a *closed circuit* configuration). In particular, we formulate a kinetic model and apply it to the investigation of the current-driven IMT in $VO_2$ to explore the possibility of the IMT entirely arising from the electron correlation weakening induced by the current, i.e., we assume an isothermal situation, which may not be readily realized in real experiments. We demonstrate that the current can indeed drive the few-nanosecond ultrafast switching through the correlation weakening effect. We further construct the temperature-current phase diagram and study the influence of the current on domain walls.

## II. METHOD

The thermodynamics of the IMT in $VO_2$ can be described by a Landau-type potential energy density functional [32, 33],

$$F_{\mathrm{t}}[T,\Phi;\{\eta_i\},\{\mu_i\},n,p] = F_0[T;\{\eta_i\},\{\mu_i\}] + F[T,\Phi;\{\mu_i\},n,p],$$

which consists of a contribution from the intrinsic $VO_2$ $F_0$ and that from additional free carriers $F$. Here $T$ is the temperature, $\Phi$ is the electric potential, $\eta_i, i=1,2,3,4$ are the structural order parameter fields, $\mu_i, i=1,2,3,4$ are the spin-correlation order parameter fields (characterizing the magnetic order), and $n$ and $p$ are the free electron and hole density fields, respectively. $\eta_i$ and $\mu_i$ explicitly characterize the structural and the electronic phase transitions during the IMT, respectively: a finite $\eta_i$ indicates the dimerization of the neighboring V atoms, and a finite $\mu_i$ indicates the formation of the dynamical singlet situated on the neighboring V sites and consequently the opening of the energy gap [2–4]. The order parameters of the different phases are: $\eta_1=\eta_3\neq 0, \eta_2=\eta_4=0, \mu_1=\mu_3\neq 0, \mu_2=\mu_4=0, \eta_1\mu_1<0, \eta_3\mu_3<0$ (and other symmetry-related values) for the M1 phase, $\eta_1\neq 0, \eta_2=\eta_3=\eta_4=0, \mu_1\neq 0, \mu_2=\mu_3=\mu_4=0, \eta_1\mu_1<0$ (and other symmetry-related values) for the M2 phase, and $\eta_i=0, \mu_i=0, i=1,2,3,4$ for the R phase [32]. The detailed form of the intrinsic Landau potential $F_0$ can be found in references [32, 33] and is also summarized in Appendix A. In the previous work [33] we employed the Boltzmann statistics commonly used in semiconductor physics as an approximation to the Fermi statistics for free electrons and holes. To better characterize the kinetics of the free electrons and holes, here we use the Fermi distribution to calculate the free electron and hole densities.

Since the energy gap opens nearly symmetrically with respect to the Fermi level of the R phase during the metal-to-insulator transition [34], we can set the energy reference to the midpoint of the gap, to simplify the description of the theory. With this reference and the simplification of one effective parabolic band for each of the conduction and the valence bands, the electron and hole densities can be written as

$$n = N_{\mathrm{c}} F_{1/2}\left(\frac{\xi_{\mathrm{e}} - E_{\mathrm{g}}/2 + e\Phi}{k_{\mathrm{B}}T}\right), \tag{1a}$$

$$p = N_{\mathrm{v}} F_{1/2}\left(\frac{\xi_{\mathrm{h}} - E_{\mathrm{g}}/2 - e\Phi}{k_{\mathrm{B}}T}\right). \tag{1b}$$

Here the function $F_{1/2}(x) \equiv (2/\sqrt{\pi})\int_0^\infty \sqrt{\epsilon}[1+\exp(\epsilon - x)]^{-1}d\epsilon$ is the Fermi integral [35]. $k_{\mathrm{B}}$ is the Boltzmann constant and $e$ is the elementary charge. $N_{\mathrm{c}} = 2(m_{\mathrm{e}}^* k_{\mathrm{B}}T/2\pi\hbar^2)^{3/2}$ and $N_{\mathrm{v}} = 2(m_{\mathrm{h}}^* k_{\mathrm{B}}T/2\pi\hbar^2)^{3/2}$ are the effective densities of states of the conduction band and the valence band, respectively, where $m_{\mathrm{e(h)}}^*$ is the effective mass of the electrons (holes) and $\hbar$ is the Planck constant over $2\pi$ [36]. $\xi_{\mathrm{e}}$ and $\xi_{\mathrm{h}}$ are the (quasi-) chemical potentials of the electrons and the holes, respectively. $E_{\mathrm{g}}$ is the gap and may be directly related to the spin-correlation order parameters [2–4] $E_{\mathrm{g}}(\{\mu_i\}) \approx 2U^2\mu_0^2\sum_i \mu_i^2/k_{\mathrm{B}}T_{\mathrm{c}}$ ($U$ is the on-site Coulomb repulsion and $\mu_0$ is a dimensionless parameter) [32, 33].

The free energy of the free electrons and holes is then just

$$F = \int\left[\int_0^n (\xi_{\mathrm{e}})_{TV}dn + \int_0^p (\xi_{\mathrm{h}})_{TV}dp\right]dV - F_{\mathrm{i}}[T;\{\mu_i\}],$$

and using Eq. (1) to eliminate the chemical potentials, one obtains

$$F = \int\left\{k_{\mathrm{B}}T\left[\int_0^n F_{1/2}^{-1}\left(\frac{n'}{N_{\mathrm{c}}}\right)dn' + \int_0^p F_{1/2}^{-1}\left(\frac{p'}{N_{\mathrm{v}}}\right)dp'\right] + \frac{E_{\mathrm{g}}}{2}(n+p) + e\Phi(p-n)\right\}dV - F_{\mathrm{i}}[T;\{\mu_i\}]. \tag{2}$$

Here $F_{1/2}^{-1}$ represents the inverse function of $F_{1/2}$ and $V$ is the volume. $F_{\mathrm{i}}$ is the equilibrium intrinsic free energy of the electrons and holes, and thus $F$ vanishes at equilibrium and zero electric field. $F_{\mathrm{i}}$ may have a complicated form. However, what is directly needed in the simulation is not $F_{\mathrm{i}}$ itself, but $\delta F_{\mathrm{i}}/\delta\mu_i$ [see Eq. (3)]. It can be proven (see Appendix B for the derivation) that $\delta F_{\mathrm{i}}/\delta\mu_i = n_{\mathrm{i}} dE_{\mathrm{g}}/d\mu_i$, where $n_{\mathrm{i}} = N_{\mathrm{c}}F_{1/2}[(\xi_{\mathrm{eq}} - E_{\mathrm{g}}/2)/k_{\mathrm{B}}T]$ is the intrinsic carrier density ($\xi_{\mathrm{eq}}$ is the equilibrium intrinsic chemical potential of the electrons).

The kinetics of the phase transition is described by the Allen-Cahn equations for the non-conserved order parameters $\eta_i$ and $\mu_i$ [37],

$$\frac{\partial\eta_i}{\partial t} = -L_\eta\frac{\delta F_{\mathrm{t}}}{\delta\eta_i}, \tag{3a}$$

$$\frac{\partial\mu_i}{\partial t} = -L_\mu\frac{\delta F_{\mathrm{t}}}{\delta\mu_i}, \tag{3b}$$

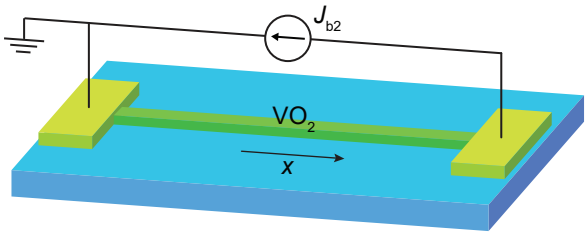


FIG. 1. Schematics of the geometry used in the simulations. The blue and the gold parts are substrate and electrodes, respectively. The length of the $VO_2$ sample is $L$, and is set to 100 nm in the simulations.

and the Cahn-Hilliard equations (diffusion equations) for the conserved order parameters $n$ and $p$ [37],

$$\frac{\partial n}{\partial t} = \nabla\cdot\left(\frac{M_e n}{e}\nabla\frac{\delta F_t}{\delta n}\right) + s, \tag{4a}$$

$$\frac{\partial p}{\partial t} = \nabla\cdot\left(\frac{M_h p}{e}\nabla\frac{\delta F_t}{\delta p}\right) + s, \tag{4b}$$

where $t$ is the time, $L_\eta$ and $L_\mu$ are constants related to the interface mobilities, $M_{e(h)}$ is the electron (hole) mobility, and $s$ is the source term representing the electron-hole recombination process. Note that in Eqs. (3-4) the natural variables of $F_t$ are $\{\eta_i\},\{\mu_i\},T,V,n,p$, and $\delta F_t/\delta n = \xi_e$ and $\delta F_t/\delta p = \xi_h$.

The source term may have the form $s = K(\{\mu_i\})(n_{eq}p_{eq} - np)$, where $n_{eq} = N_c F_{1/2}[(\xi_{eq} - E_g/2 + e\Phi)/k_BT]$ and $p_{eq} = N_v F_{1/2}[(-\xi_{eq} - E_g/2 - e\Phi)/k_BT]$ are the equilibrium densities of the electrons and the holes, respectively, and $K$ is the recombination rate coefficient independent of $n$ and $p$. In the insulating phase, $K$ is finite. In the metallic phase, however, $K$ should be zero: the holes appearing in the metallic phase in the model are not the genuine holes as in the insulating phase, but rather should be interpreted as an effective positive-charge background for the free electrons to achieve charge neutrality, in which case the concept of the electron-hole recombination is not applicable. To account for this, we assume the symmetry-allowed lowest order dependence of $K$ on the electronic order parameters, $K = K_0\sum_i \mu_i^2$, where $K_0$ is a constant.

Equations (3,4) are closed by the Poisson equation for the self-consistent determination of the electric potential $\Phi$,

$$-\nabla^2\Phi = \frac{e(p-n)}{\epsilon_0\epsilon_r},$$

where $\epsilon_0$ and $\epsilon_r$ are the vacuum dielectric permittivity and the relative dielectric permittivity of $VO_2$, respectively. In the simulations, for Eq. (4) we use the energies $\gamma_e \equiv \xi_e - E_g/2 + e\Phi$ and $\gamma_h \equiv \xi_h - E_g/2 - e\Phi$ as the unknown variables instead of $n$ and $p$, and obtain $n$ and $p$ through Eq. (1) after solving for $\gamma_e$ and $\gamma_h$.

The boundary conditions are schematically represented in Fig. 1. The left boundary ($x = 0$) is connected to the ground, i.e., we have

$$\Phi|_{x=0} = 0,$$
$$\gamma_e|_{x=0} = \gamma_h|_{x=0} = \gamma_{b1},$$

where $\gamma_{b1}$ is a constant corresponding to a fixed carrier density $n_{b1}$ at the boundary, $n|_{x=0} = p|_{x=0} = n_{b1}$. The right boundary ($x = L$) has a constant flux. We assume that the boundary condition for $\Phi$ at $x = L$ corresponds to a small constant electric field in the electrode $E_{lctrd2}$ (we set $E_{lctrd2}$ to 0.001 MV/m). Eventually we have,

$$(\partial_x\Phi)|_{x=L} + E_{lctrd2} = \frac{e(p-n)|_{x=L}\lambda}{\epsilon_0\epsilon_r},$$
$$j_e|_{x=L} = -\frac{J_{b2}}{e},\ j_h|_{x=L} = 0,$$

where $\lambda$ is the length of the charge depletion region at the boundary and is set to 5 nm, $j_e = -(M_e n/e)\partial_x\xi_e$ [$j_h = -(M_h p/e)\partial_x\xi_h$] is the electron (hole) flux, and $J_{b2}$ is the constant boundary current density. In the simulations we find that different values of $E_{lctrd2}$ and $\lambda$ have minor influence on the results. We assume Neumann boundary condition for the order parameters $\eta_i$ and $\mu_i$ at both boundaries, i.e., $(\partial_x\eta_i)|_{x=0,L} = (\partial_x\mu_i)|_{x=0,L} = 0$, which corresponds to no interaction of the order parameters at boundaries.

We estimate the parameters in the model based on experimental results. To our best knowledge, the hole mobility in $VO_2$ has not yet been directly measured. Nonetheless, we estimate the ratio of the electron and hole mobilities $M_e/M_h \approx 1.2$ from the position of the photocurrent peak in the scanning photocurrent microscopy measurement [34]. The constant characterizing the electron-hole recombination rate $K_0$ can be calculated from the free carrier lifetime $\tau_{eh} \sim 10$ $\mu$s [34] through the relation $K_0 = (2n_{ic}\tau_{eh})^{-1}$ [41], where $n_{ic}$ is the intrinsic carrier density of the insulating phase near $T_c$ (note that $\sum_i \mu_i^2 \sim 1$ in the insulating phase). Similarly, $L_\eta$ and $L_\mu$ can be estimated from the characterization times of the structural and the electronic phase transitions $\tau_\eta \sim 1$ ps [15] and $\tau_\mu \sim 10$ fs [24], by $L_\eta \sim [\tau_\eta a(T_c - T_1)/T_c]^{-1}$ and $L_\mu \sim (4U^2\mu_0^2 n_{ex}\tau_\mu/k_BT_c)^{-1}$, respectively. Here $a$ and $T_1$ are the Landau coefficient and the "Curie-Weiss temperature" of the quadratic term of

TABLE I. Values of the parameters estimated from experiments. $m_e$ is the electron mass.

| $m^*_{e,h}$ ($m_e$) [38] | $M_e$ ($cm^2$/Vs) [39] | $\frac{M_e}{M_h}$ [34] | $K_0$ ($cm^3$/s) [34] | $L_\eta$ ($cm^3$/Js) [15] | $L_\mu$ ($cm^3$/Js) [24] | $\epsilon_r$ [40] |
|---|---|---|---|---|---|---|
| 65 | 0.5 | 1.2 | $6.8\times10^{-17}$ | $3.3\times10^{10}$ | $2.0\times10^{11}$ | 60[a] |

[a] $\epsilon_r$ varies appreciably with temperature. However we observe that different values of $\epsilon_r$ have minor influence on the switching behavior, e.g., the switching times for $\epsilon_r \sim 40$ (near room temperature) and for $\epsilon_r \sim 100$ (near 320 K) at temperature 320 K and current density 57.8 nA/$nm^2$ differ within 2%.

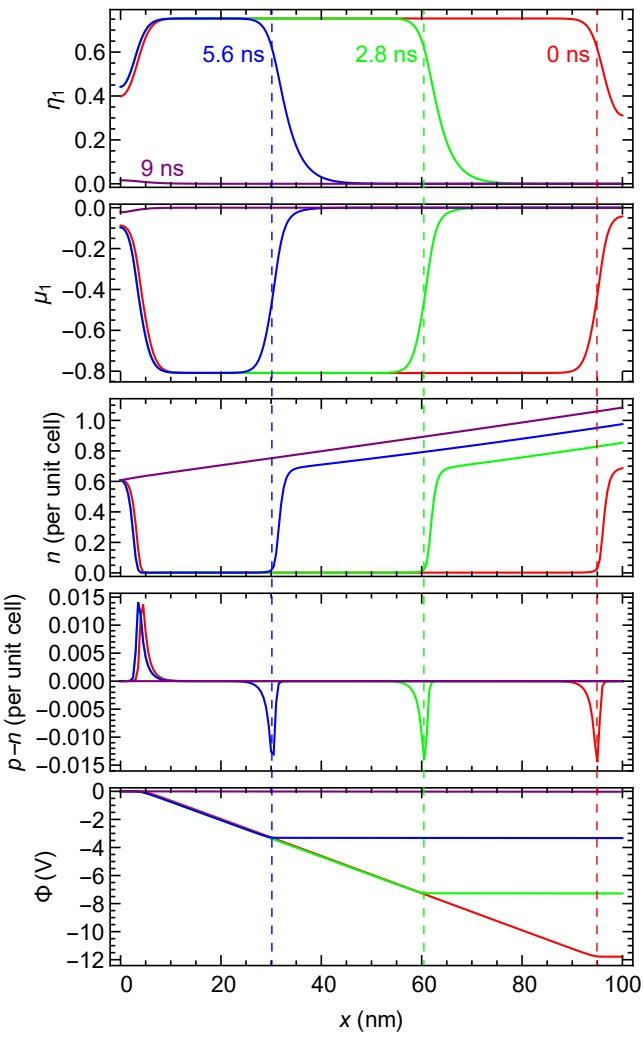


FIG. 2. Simulated temporal evolution of various variables during the current-driven ultrafast switching in $VO_2$ at $T = 320$ K, $J_{b2} = 57.8$ nA/nm$^2$ and $n_{b1} \approx 0.6$ per unit cell. During the process, $\eta_3$ ($\mu_3$) is the same as $\eta_1$ ($\mu_1$), and $\eta_2 = \eta_4 = 0$ and $\mu_2 = \mu_4 = 0$. The dashed lines indicate the positions of the insulator-metal interface at different times.

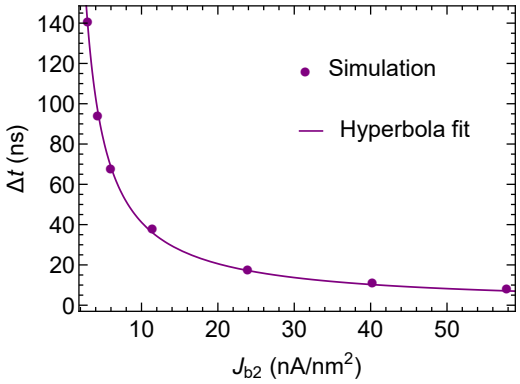


FIG. 3. Switching time as a function of the current density in $VO_2$ at $T = 320$ K. The line is the hyperbola fit to the simulation data, $\Delta t = c/J_{b2}$, with the fitted constant $c = 412$ ns · nA/nm$^2$.

$\eta_i$, respectively (see Appendix A), and $n_{ex} \approx 0.08$ per V atom is the photoexcited free electron density in the measurement of $\tau_\mu$ [24]. The values of the parameters estimated from experiments are summarized in Table I.

## III. CURRENT-DRIVEN ULTRAFAST SWITCHING AND PHASE DIAGRAM

We first investigate the case in which the $VO_2$ sample has an initial equilibrium M1 phase in the bulk and is subject to a large current density $\sim 10^1$ nA/nm$^2$. This could be the case in the measurements of the voltage-pulse-induced ultrafast switching in $VO_2$ [17, 19, 20]. Figure 2 shows the calculated temporal evolution of various variables at $T = 320$ K, $J_{b2} = 57.8$ nA/nm$^2$ and $n_{b1} \approx 0.6$ per unit cell. We find that $n_{b1}$ has minor influence on the profiles of the variables in the bulk and on the switching time. At $t = 0$ ns, the structural order parameters and the electronic order parameters have uniform equilibrium finite values $\eta_1 = \eta_3 = 0.76$ and $\mu_1 = \mu_3 = -0.84$ in the bulk ($\eta_2 = \eta_4 = 0$ and $\mu_2 = \mu_4 = 0$), indicating the initial state is a uniform monoclinic insulator (M1 phase). $\eta_1$ ($\eta_3$) and $\mu_1$ ($\mu_3$) then turn to zero from the $x = L$ end, representing that the rutile metal (R phase) grows from the $x = L$ end. This is in contrast to the Joule-heating-induced switching, in which the initial insulator turns into the metal uniformly due to the uniform heating. The metallic phase spreads from the $x = L$ end to the $x = 0$ end in $\sim 9$ ns, yielding a few-nanosecond ultrafast switching. This is consistent with the 4 ns switching time (scaled to a 100-nm-long $VO_2$ sample) observed in the voltage-pulse-induced IMT in $VO_2$ at a peak current density on the order of $10^{1\sim2}$ nA/nm$^2$ [17].

Compared to the IMT induced by the photoexcited electrons in the optical experiments [15, 24], the growth of the metallic phase from the $x = L$ end is driven by the carrier doping from the carrier injection and the negative electric potential [6, 33]. The excess carriers screen the electron-electron repulsion and thus reduce the electron correlation (the electronic order parameters), thereby stabilize the metallic phase [22–24]. As the metallic phase grows, there are net negative charges accumulating at the insulator-metal interface. The electric potential becomes flat inside the metallic phase as expected.

The switching time $\Delta t$ depends on the current density. Figure 3 presents $\Delta t$ as a function of the applied current density $J_{b2}$, showing that $\Delta t$ decreases as $J_{b2}$ increases. $\Delta t(J_{b2})$ is well fitted by a hyperbola function, $\Delta t = c/J_{b2}$, with $c = 412$ ns · nA/nm$^2$. Since the metallic phase grows from one end to another, $J_{b2}$ is then seen proportional to the average growth speed of the metallic phase, implying that the switching is controlled by the carrier dynamics (not the phase transformation dynam-

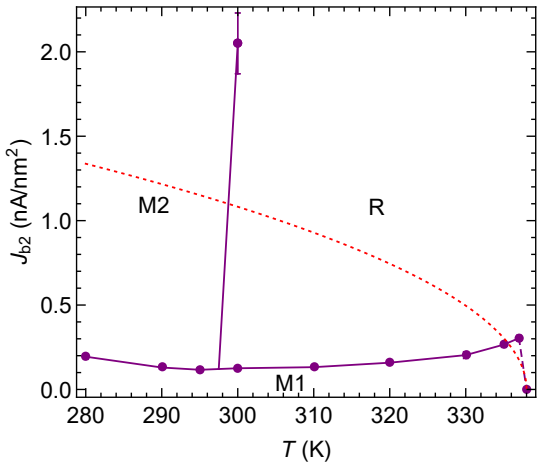


FIG. 4. Calculated temperature versus current density phase diagram of $VO_2$. The dots with error bars are the calculated points on the phase boundaries (the presence of the error bars results from the discretely sampled calculation points on the phase diagram), and the lines are guide to eyes. The dashed line represents the discontinuous point. The red dotted line is the boundary line for the Joule-heating-induced IMT: for $J_{b2}$ exceeding this line, the R phase will eventually be induced by the Joule heating effect (see text).

ics). It can be interpreted by the fact that the characteristic times of the electronic and the structural phase transitions $\tau_\mu$ and $\tau_\eta$, are much shorter than the time for the carrier density at the metal-insulator interface to reach the metallic value, $\tau_0$. $\tau_0$ can be estimated to be $\tau_0 \approx d_0/v_0 \approx 0.4$ ns which is indeed much longer than $\tau_\mu$ and $\tau_\eta$, where $v_0 \approx 13$ m/s is the average growth speed of the metallic phase and $d_0 \approx 5$ nm is half of the interface width (see Fig. 2). This further implies that the switching behavior is insensitive to $\tau_\eta$ and $\tau_\mu$ as long as $\tau_\eta$ and $\tau_\mu$ do not vary by many orders of magnitude. The fitting function can be used to calculate the switching time at large current densities, e.g., $\Delta t = 0.2$ ns at $J_{b2} = 2 \times 10^3$ nA/nm$^2$, which is comparable to the 0.48 ns switching time (scaled to a 100-nm-long $VO_2$ sample) found in the voltage-pulse-induced IMT in $VO_2$ at a peak current density of the same magnitude [19].

Knowing that the current can induce the IMT isothermally, we further calculate the temperature versus current density phase diagram of $VO_2$ under the isothermal condition. The result is shown in Fig. 4. It should be noted that any point on the phase diagram corresponds to a nonequilibrium steady state, not an equilibrium stable state. Strikingly, the simulation suggests that the current may induce the M2 phase at low temperatures ($< 298$ K). The M2-R phase boundary has a large positive slope, indicating that a current with large enough density may eventually drive the M1 phase to the M2 phase even at high temperatures ($> 298$ K).

Nonetheless, in practice the Joule heating effect may set a boundary line in the phase diagram, beyond which it governs the IMT. The criterion for the onset of the Joule-heating-induced IMT depends on the sample geometry and heat dissipation to surroundings. For the geometry shown in Fig. 1, we consider that the heat generated in $VO_2$ is mainly dissipated through the substrate. At steady state, the critical current density for the onset of the Joule-heating-induced IMT $J_{Jc}$ is simply determined by the balance between the electric power and the heat dissipation,

$$\frac{J_{Jc}^2}{\sigma} = \frac{h}{D}(T_c - T_s), \tag{5}$$

where $\sigma = 4.6 \times 10^3$ S/m is the conductivity of the insulating phase of $VO_2$ at $T_c$ [42], $h \sim 6.7 \times 10^5$ W/Km$^2$ is the effective heat transfer coefficient for a 100-nm-thick $VO_2$ film in contact with a sapphire substrate [27], $D$ is the thickness of the $VO_2$ nanobeam (perpendicular to the substrate plane), and $T_s$ is the temperature of the substrate (also considered as the initial temperature of the $VO_2$ sample). $J_{Jc}$ as a function of $T_s$ from Eq. (5) for a typical $D = 100$ nm is also plotted in Fig. 4 as a red dotted line. Therefore, in a typical 100-nm-thick $VO_2$ film/nanobeam on sapphire substrate, the Joule heating will eventually induce the R phase for $J_{b2}$ exceeding the boundary line $J_{Jc}(T_s)$. We note that for polycrystalline $VO_2$, $J_{Jc}$ could be dramatically suppressed due to the suppressed conductivity.

The critical current density of the M1-R phase transition increases at elevating temperature, which finally leads to the presence of a discontinuous point at $T_c$, as shown by the dashed line in Fig. 4. This may be interpreted as follows. The growth of the metallic phase is driven by the carrier accumulation at the metal-insulator interface. In the insulator side, a higher temperature (below $T_c$) leads to a higher carrier density, resulting in a larger current density there. Hence, in order for free electrons to accumulate at the metal-insulator interface at a higher temperature, the current density must be larger in the metal side (exceeding the current density in the insulator side). In practice the discontinuous point in the phase diagram should not present. When the temperature approaches $T_c$, $J_{Jc}$ will be smaller than the critical $J_{b2}$ (Fig. 4), meaning that the Joule heating effect controls the IMT there. Thus the critical current density will practically follow $J_{Jc}$ and drop to zero continuously when $T \to T_c$.

## IV. CURRENT-DRIVEN DOMAIN WALL MOTION

We then examine how the current affects the domain wall in $VO_2$. The initial configuration is set to a two-domain structure within the M1 phase, with the domain wall (twin wall) located at $x = L/2$. This is shown by the profiles of $\eta_3$ and $\mu_3$ at $t = 0$ ns in Fig. 5. The order parameters of the right domain are $\eta_1 = \eta_3 = 0.76, \eta_2 = \eta_4 = 0, \mu_1 = \mu_3 = -0.84, \mu_2 = \mu_4 = 0$, which is denoted

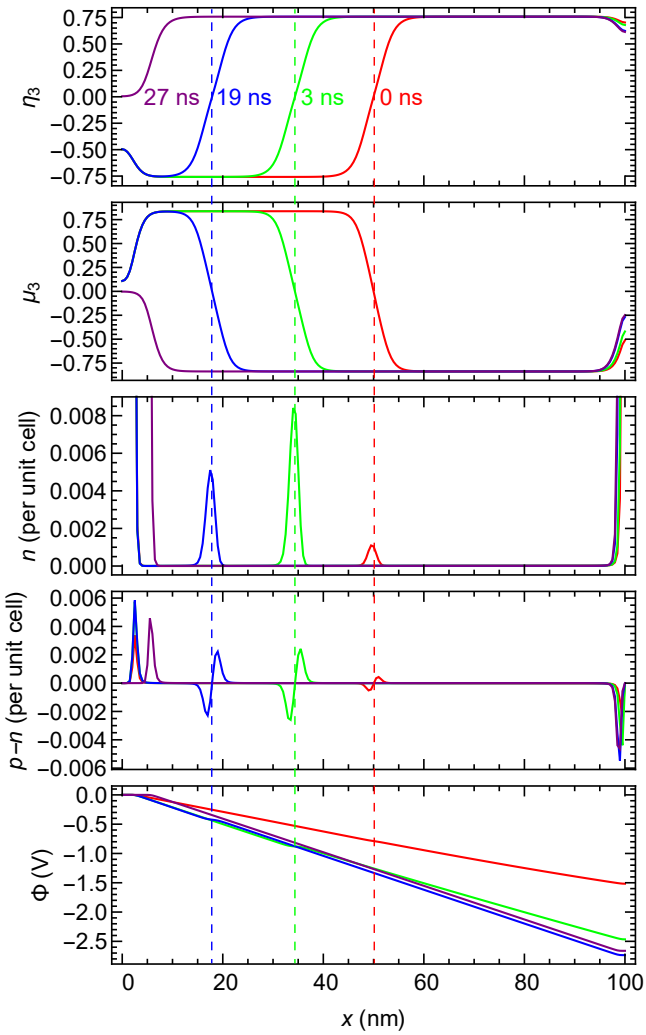


FIG. 5. Simulated temporal evolution of various variables during the current-driven domain wall motion in $VO_2$ at $T = 320$ K, $J_{b2} = 0.0811$ nA/nm$^2$ and $n_{b1} \approx 0.6$ per unit cell. During the process, $\eta_1$ ($\mu_1$) has a nearly uniform value 0.76 ($-0.84$) along the sample despite at the boundaries, and $\eta_2 = \eta_4 = 0$ and $\mu_2 = \mu_4 = 0$. The dashed lines indicate the positions of the twin wall within the M1 phase at different times. The range of the finite net charge region at $x = L$ boundary is within $\lambda \triangleq 5$ nm, which justifies this setting of $\lambda$.

as the variant 1 of the M1 phase. The order parameters of the left domain are $\eta_1 = -\eta_3 = 0.76, \eta_2 = \eta_4 = 0, \mu_1 = -\mu_3 = -0.84, \mu_2 = \mu_4 = 0$, which corresponds to a 180° rotation about the rutile $c$ axis of the variant 1, and is denoted as the variant 3 of the M1 phase. As can be seen in Fig. 5, upon the application of a current with a small density (not adequate to trigger the IMT), the twin wall between the variant 1 and the variant 3 moves opposite to the current direction (i.e., $-x$ direction), and finally moves to the $x = 0$ end in less than 27 ns, leading to the vanishing of the variant 3.

The twin wall has a relatively large carrier density, and thus a relatively large conductivity compared to the interior of the domains. The net charges localized at the twin wall form an effective dipole oriented along the direction of the electric field. Due to the same reason discussed in the current-driven switching, the twin wall motion speed is insensitive to $\tau_\mu$ and $\tau_\eta$.

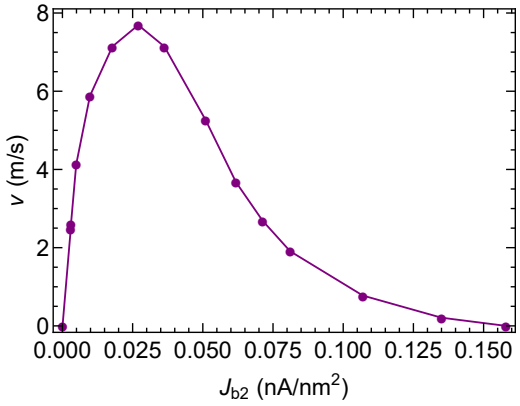


FIG. 6. Average speed of the twin wall motion from $x = 50$ nm to $x = 0$ nm as a function of the current density in $VO_2$ at $T = 320$ K. The line is guide to eyes.

Similar to the current-driven resistive switching, the current density affects the speed of the twin wall motion. Figure 6 shows the average speed, $v$, of the twin wall motion from $x = 50$ nm to $x = 0$ nm as a function of the current density. $v$ first increases, and then decreases as the current density increases. It reaches its maximum at $J_{b2} \sim 0.026$ nA/nm$^2$ and approaches zero when $J_{b2}$ approaches the critical value for triggering the IMT. The reason why $v$ decreases with increasing $J_{b2}$ at large $J_{b2}$ is as follows. $v$ should be proportional to the carrier accumulation rate in front of the twin wall, $v \propto (\partial_t n)|_{x_0-d/2}$, where $x_0$ denotes the position of the twin wall and $d$ is the twin wall thickness. But we have $(\partial_t n)|_{x_0-d/2} \sim -2[j_e(x_0) - j_e(x_0 - d/2)]/d$, where $j_e \sim -M_e n E$ ($E$ is the electric field). Hence $(\partial_t n)|_{x_0-d/2} \sim 2M_e[n(x_0)E(x_0) - n(x_0 - d/2)E(x_0 - d/2)]/d$. From the Poisson equation, the electric fields at $x_0$ and $x_0 - d/2$ have a relation, $2[E(x_0) - E(x_0 - d/2)]/d \approx \rho_0/\epsilon_0\epsilon_r$, where $\rho_0 < 0$ is the net charge density at $x_0 - d/2$ [see $(p - n)$ profile in Fig. 5]. Then we have

$$v \propto \left[n(x_0) - n\left(x_0 - \frac{d}{2}\right)\right] E\left(x_0 - \frac{d}{2}\right) + \frac{n(x_0)\rho_0 d}{2\epsilon_0\epsilon_r}.$$

The increasing $J_{b2}$ leads to the increase in $E(x_0 - d/2)$ [note that $n(x_0) - n(x_0 - d/2) > 0$], while the increased electric field leads to a stronger electron-hole separation near the twin wall, thus resulting in a smaller $\rho_0$ (more negative). These two competing effects lead to the eventual drop of $v$ as $J_{b2}$ increases.

We note that this current-driven twin wall motion cannot be realized via the Joule heating effect, since the Joule heating effect is symmetric about $\pm x$ directions.

## V. CONCLUSION

We formulated a phase-field model that takes into account the structural distortion, the electron correlation and the free carriers to describe the mesoscale kinetics of the IMT in strongly correlated $VO_2$. We applied it to the investigation of the isothermal current-driven IMT in $VO_2$. The simulation showed that the free electrons injected by a current with large density reduce the electron correlation (electronic order parameter $\mu_i$) and lead to a few-nanosecond ultrafast resistive switching isothermally. The obtained temperature versus current density phase diagram indicates that the current may induce the M2 phase at low temperatures under the isothermal condition. The current was also shown to be able to drive the domain wall to move, which could potentially be employed to transform a multi-domain sample to the single-domain state. This theoretical framework could be utilized to simulate other phase transition processes in mesoscale $VO_2$ systems subject to various external stimuli, and may be extended to other strongly correlated materials exhibiting IMT.

## ACKNOWLEDGMENTS

This work was funded by the Penn State MRSEC, Center for Nanoscale Science, under the award NSF DMR-1420620.

### Appendix A: expression for $F_0$

The intrinsic Landau potential $F_0$ consists of a bulk energy term $f_\mathrm{b}$ and a gradient energy term $f_\mathrm{g}$ [32, 33],

$$F_0 = \int [f_\mathrm{b}(T;\{\eta_i\},\{\mu_i\}) + f_\mathrm{g}(\{\eta_i\},\{\mu_i\})]dV,$$

where $dV$ is the infinitesimal volume element. $f_\mathrm{b}$ can be constructed from symmetry analysis [32],

$$\begin{aligned} f_\mathrm{b} =& \frac{a(T-T_1)}{2T_\mathrm{c}}\eta_i\eta_i + \frac{b_{ij}}{4}\eta_i^2\eta_j^2 + \frac{c_{ij}}{6}\eta_i^2\eta_j^4 \\ &+ \frac{A(T-T_2)}{2T_\mathrm{c}}\mu_i\mu_i + \frac{B_{ij}}{4}\mu_i^2\mu_j^2 + \frac{C_{ij}}{6}\mu_i^2\mu_j^4 \\ &+ h\eta_i\mu_i - \frac{p_{ijkl}}{2}\eta_i\eta_j\mu_k\mu_l + \frac{q_{ijkl}}{2}\eta_i\eta_j\eta_k\mu_l, \end{aligned}$$

where $T_1$ and $T_2$ are the "Curie-Weiss temperatures" of the structural and the electronic order parameters, respectively, and $a$, $b$'s, $c$'s, $A$, $B$'s, $C$'s, $h$, $p$'s and $q$'s are constants satisfying certain symmetry relations [32]. The Einstein summation convention is used. We assume an isotropic form for $f_\mathrm{g}$ [33, 43],

$$f_\mathrm{g} = \frac{\kappa_1}{2}(\nabla\eta_i)\cdot(\nabla\eta_i) + \frac{\kappa_2}{2}(\nabla\mu_i)\cdot(\nabla\mu_i),$$

where $\kappa$'s are positive constants.

### Appendix B: derivation of $\delta F_\mathrm{i}/\delta\mu_i$

Let us first denote the integral in Eq. (2) at $\Phi = 0$ as $F^0[\{\mu_i\}, n, p]$. Then by definition $F_\mathrm{i}[\{\mu_i\}] = F^0|_{n,p=n_\mathrm{i}}$. Since $F_\mathrm{i}$ depends on $\mu_i$ only through $E_\mathrm{g}(\{\mu_i\})$, we obtain

$$\frac{\delta F_\mathrm{i}}{\delta\mu_i} = \frac{\delta F_\mathrm{i}}{\delta E_\mathrm{g}}\frac{dE_\mathrm{g}}{d\mu_i}. \tag{B1}$$

We also have

$$\frac{\delta F_\mathrm{i}}{\delta E_\mathrm{g}} = \frac{\delta F^0}{\delta E_\mathrm{g}}\bigg|_{n,p=n_\mathrm{i}} + \left(\frac{\delta F^0}{\delta n} + \frac{\delta F^0}{\delta p}\right)\bigg|_{n,p=n_\mathrm{i}}\frac{dn_\mathrm{i}}{dE_\mathrm{g}}.$$

But $(\delta F^0/\delta E_\mathrm{g})|_{n,p=n_\mathrm{i}} = n_\mathrm{i}$, and the equilibrium conditions are $(\delta F^0/\delta n)|_{n,p=n_\mathrm{i}} = \xi_\mathrm{e} = \xi_\mathrm{eq}$ and $(\delta F^0/\delta p)|_{n,p=n_\mathrm{i}} = \xi_\mathrm{h} = -\xi_\mathrm{eq}$ [33]. We thus have

$$\frac{\delta F_\mathrm{i}}{\delta E_\mathrm{g}} = n_\mathrm{i}.$$

The substitution of this equation in Eq. (B1) just gives the desired relation

$$\frac{\delta F_\mathrm{i}}{\delta\mu_i} = n_\mathrm{i}\frac{dE_\mathrm{g}}{d\mu_i}.$$

This completes the proof.

[1] F. J. Morin, "Oxides Which Show a Metal-to-Insulator Transition at the Neel Temperature," Phys. Rev. Lett. **3**, 34–36 (1959).
[2] S. Biermann, A. Poteryaev, A. I. Lichtenstein, and A. Georges, "Dynamical Singlets and Correlation-Assisted Peierls Transition in $VO_2$," Phys. Rev. Lett. **94**, 026404 (2005).
[3] Huihuo Zheng and Lucas K. Wagner, "Computation of the Correlated Metal-Insulator Transition in Vanadium Dioxide from First Principles," Phys. Rev. Lett. **114**, 176401 (2015).
[4] W. H. Brito, M. C. O. Aguiar, K. Haule, and G. Kotliar, "Metal-Insulator Transition in $VO_2$: A DFT + DMFT Perspective," Phys. Rev. Lett. **117**, 056402 (2016).

[5] Feiyi Liao, Zheng Zhu, Zhuocheng Yan, Guang Yao, Zhenlong Huang, Min Gao, Taisong Pan, Yin Zhang, Qiang Li, Xue Feng, and Yuan Lin, "Ultrafast response flexible breath sensor based on vanadium dioxide," Journal of Breath Research **11**, 036002 (2017).

[6] M. Nakano, K. Shibuya, D. Okuyama, T. Hatano, S. Ono, M. Kawasaki, Y. Iwasa, and Y. Tokura, "Collective bulk carrier delocalization driven by electrostatic surface charge accumulation," Nature **487**, 459 (2012).

[7] Myungwoo Son, Joonmyoung Lee, Jubong Park, Jungho Shin, Godeuni Choi, Seungjae Jung, Wootae Lee, Seonghyun Kim, Sangsu Park, and Hyunsang Hwang, "Excellent Selector Characteristics of Nanoscale $VO_2$ for High-Density Bipolar ReRAM Applications," Electron Device Letters, IEEE **32**, 1579–1581 (2011).

[8] T. Driscoll, H.-T. Kim, B.-G. Chae, M. Di Ventra, and D. N. Basov, "Phase-transition driven memristive system," Applied Physics Letters **95**, 043503 (2009).

[9] Zheng Yang, Changhyun Ko, and Shriram Ramanathan, "Oxide Electronics Utilizing Ultrafast Metal-Insulator Transitions," Annual Review of Materials Research **41**, 337–367 (2011).

[10] Jae Hyung Park, Jim M. Coy, T. Serkan Kasirga, Chunming Huang, Zaiyao Fei, Scott Hunter, and David H. Cobden, "Measurement of a solid-state triple point at the metal-insulator transition in $VO_2$," Nature **500**, 431–434 (2013).

[11] A. Zylbersztejn and N. F. Mott, "Metal-insulator transition in vanadium dioxide," Phys. Rev. B **11**, 4383–4395 (1975).

[12] Elizabeth E. Chain, "Optical properties of vanadium dioxide and vanadium pentoxide thin films," Appl. Opt. **30**, 2782–2787 (1991).

[13] M. Marezio, D. B. McWhan, J. P. Remeika, and P. D. Dernier, "Structural Aspects of the Metal-Insulator Transitions in Cr-Doped $VO_2$," Phys. Rev. B **5**, 2541–2551 (1972).

[14] J. P. Pouget, H. Launois, J. P. D'Haenens, P. Merenda, and T. M. Rice, "Electron Localization Induced by Uniaxial Stress in Pure $VO_2$," Phys. Rev. Lett. **35**, 873–875 (1975).

[15] A. Cavalleri, Cs. Tóth, C. W. Siders, J. A. Squier, F. Ráksi, P. Forget, and J. C. Kieffer, "Femtosecond Structural Dynamics in $VO_2$ during an Ultrafast Solid-Solid Phase Transition," Phys. Rev. Lett. **87**, 237401 (2001).

[16] B. Wu, A. Zimmers, H. Aubin, R. Ghosh, Y. Liu, and R. Lopez, "Electric-field-driven phase transition in vanadium dioxide," Phys. Rev. B **84**, 241410 (2011).

[17] J. Leroy, A. Crunteanu, A. Bessaudou, F. Cosset, C. Champeaux, and J.-C. Orlianges, "High-speed metal-insulator transition in vanadium dioxide films induced by an electrical pulsed voltage over nano-gap electrodes," Applied Physics Letters **100**, 213507 (2012).

[18] Giwan Seo, Bong-Jun Kim, Changhyun Ko, Yanjie Cui, Yong Lee, Jun-Hwan Shin, Shriram Ramanathan, and Hyun-Tak Kim, "Voltage-Pulse-Induced Switching Dynamics in $VO_2$ Thin-Film Devices on Silicon," Electron Device Letters, IEEE **32**, 1582–1584 (2011).

[19] You Zhou, X. N. Chen, C. H. Ko, Zheng Yang, Chandra Mouli, and Shriram Ramanathan, "Voltage-Triggered Ultrafast Phase Transition in Vanadium Dioxide Switches," IEEE Electron Device Letters **34**, 220–222 (2013).

[20] Byung-Gyu Chae, Hyun-Tak Kim, Doo-Hyeb Youn, and Kwang-Yong Kang, "Abrupt metal–insulator transition observed in $VO_2$ thin films induced by a switching voltage pulse," Physica B: Condensed Matter **369**, 76–80 (2005).

[21] Yoshiaki Taketa and Ryoichi Furugochi, "Switching and oscillation phenomena in $SnO_2$-$VO_x$-PdO ceramics," Applied Physics Letters **31**, 405–406 (1977).

[22] Hyun-Tak Kim, Byung-Gyu Chae, Doo-Hyeb Youn, Sung-Lyul Maeng, Gyungock Kim, Kwang-Yong Kang, and Yong-Sik Lim, "Mechanism and observation of Mott transition in $VO_2$-based two-and three-terminal devices," New Journal of Physics **6**, 52 (2004).

[23] G. Stefanovich, A. Pergament, and D. Stefanovich, "Electrical switching and Mott transition in $VO_2$," Journal of Physics: Condensed Matter **12**, 8837 (2000).

[24] Daniel Wegkamp, Marc Herzog, Lede Xian, Matteo Gatti, Pierluigi Cudazzo, Christina L. McGahan, Robert E. Marvel, Richard F. Haglund, Angel Rubio, Martin Wolf, and Julia Stähler, "Instantaneous Band Gap Collapse in Photoexcited Monoclinic $VO_2$ due to Photocarrier Doping," Phys. Rev. Lett. **113**, 216401 (2014).

[25] Bongjin Simon Mun, Joonseok Yoon, Sung-Kwan Mo, Kai Chen, Nobumichi Tamura, Catherine Dejoie, Martin Kunz, Zhi Liu, Changwoo Park, Kyungsun Moon, and Honglyoul Ju, "Role of joule heating effect and bulk-surface phases in voltage-driven metal-insulator transition in $VO_2$ crystal," Applied Physics Letters **103**, 061902 (2013).

[26] Iuliana P. Radu, B. Govoreanu, S. Mertens, X. Shi, M. Cantoro, M. Schaekers, M. Jurczak, Stefan De Gendt, Andre Stesmans, J. A. Kittl, and Others, "Switching mechanism in two-terminal vanadium dioxide devices," Nanotechnology **26**, 165202 (2015).

[27] S. B. Lee, K. Kim, J. S. Oh, B. Kahng, and J. S. Lee, "Origin of variation in switching voltages in threshold-switching phenomena of $VO_2$ thin films," Applied Physics Letters **102**, 063501 (2013).

[28] A. Zimmers, L. Aigouy, M. Mortier, A. Sharoni, Siming Wang, K. G. West, J. G. Ramirez, and Ivan K. Schuller, "Role of Thermal Heating on the Voltage Induced Insulator-Metal Transition in $VO_2$," Phys. Rev. Lett. **110**, 056601 (2013).

[29] Dasheng Li, Abhishek A. Sharma, Darshil K. Gala, Nikhil Shukla, Hanjong Paik, Suman Datta, Darrell G. Schlom, James A. Bain, and Marek Skowronski, "Joule Heating-Induced Metal–Insulator Transition in Epitaxial $VO_2$/$TiO_2$ Devices," ACS Applied Materials & Interfaces **8**, 12908–12914 (2016).

[30] Arash Joushaghani, Junho Jeong, Suzanne Paradis, David Alain, J. Stewart Aitchison, and Joyce K. S. Poon, "Voltage-controlled switching and thermal effects in $VO_2$ nano-gap junctions," Applied Physics Letters **104**, 221904 (2014).

[31] Zheng Yang, Sean Hart, Changhyun Ko, Amir Yacoby, and Shriram Ramanathan, "Studies on electric triggering of the metal-insulator transition in $VO_2$ thin films between 77 K and 300 K," Journal of Applied Physics **110**, 033725 (2011).

[32] Yin Shi, Fei Xue, and Long-Qing Chen, "Ginzburg-Landau theory of metal-insulator transition in $VO_2$: The electronic degrees of freedom," Europhysics Letters **120**, 46003 (2017).

[33] Yin Shi and Long-Qing Chen, "Phase-field model of insulator-to-metal transition in $VO_2$ under an electric field," Phys. Rev. Materials **2**, 053803 (2018).

[34] Chris Miller, Mark Triplett, Joel Lammatao, Joonki Suh, Deyi Fu, Junqiao Wu, and Dong Yu, "Unusually long free carrier lifetime and metal-insulator band offset in vanadium dioxide," Phys. Rev. B **85**, 085111 (2012).

[35] Anna N. Morozovska, Eugene A. Eliseev, Olexandr V. Varenyk, Yunseok Kim, Evgheni Strelcov, Alexander Tselev, Nicholas V. Morozovsky, and Sergei V. Kalinin, "Nonlinear space charge dynamics in mixed ionic-electronic conductors: Resistive switching and ferroelectric-like hysteresis of electromechanical response," Journal of Applied Physics **116**, 066808 (2014).

[36] John L. Moll, *Physics of semiconductors* (McGraw-Hill, New York, 1964).

[37] Long-Qing Chen, "Phase-field models for microstructure evolution," Annual review of materials research **32**, 113–140 (2002).

[38] Deyi Fu, Kai Liu, Tao Tao, Kelvin Lo, Chun Cheng, Bin Liu, Rong Zhang, Hans A. Bechtel, and Junqiao Wu, "Comprehensive study of the metal-insulator transition in pulsed laser deposited epitaxial $VO_2$ thin films," Journal of Applied Physics **113**, 043707 (2013).

[39] W. H. Rosevear and W. Paul, "Hall Effect in $VO_2$ near the Semiconductor-to-Metal Transition," Phys. Rev. B **7**, 2109–2111 (1973).

[40] Zheng Yang, Changhyun Ko, Viswanath Balakrishnan, Gokul Gopalakrishnan, and Shriram Ramanathan, "Dielectric and carrier transport properties of vanadium dioxide thin films across the phase transition utilizing gated capacitor devices," Phys. Rev. B **82**, 205101 (2010).

[41] W. Shockley and W. T. Read, "Statistics of the Recombinations of Holes and Electrons," Phys. Rev. **87**, 835–842 (1952).

[42] Sangwook Lee, Kedar Hippalgaonkar, Fan Yang, Jiawang Hong, Changhyun Ko, Joonki Suh, Kai Liu, Kevin Wang, Jeffrey J. Urban, Xiang Zhang, Chris Dames, Sean A. Hartnoll, Olivier Delaire, and Junqiao Wu, "Anomalously low electronic thermal conductivity in metallic vanadium dioxide," Science **355**, 371–374 (2017).

[43] D. Lee, B. Chung, Y. Shi, G.-Y. Kim, N. Campbell, F. Xue, K. Song, S.-Y. Choi, J. P. Podkaminer, T. H. Kim, P. J. Ryan, J.-W. Kim, T. R. Paudel, J.-H. Kang, D. A. Tenne, E. Y. Tsymbal, M. S. Rzchowski, L. Q. Chen, J. Lee, and C. B. Eom, "Isostructural metal-insulator transition," Science **362**, 1037–1040 (2018).